



PCCP

Role of Cationic Group in Defining Structural and Dynamic Correlations in Anion Exchange Membranes: A Molecular Dynamics Simulation Study of Hydrated Quaternary Ammonium-functionalized Poly (p-phenylene oxide)-based Membranes

Journal:	<i>Physical Chemistry Chemical Physics</i>
Manuscript ID	CP-ART-04-2018-002211.R1
Article Type:	Paper
Date Submitted by the Author:	22-Jun-2018
Complete List of Authors:	Dong, Dengpan; University of Utah Wei, Xiaoyu; University of Utah, Materials Science & Engineering Hooper, Justin; University of Utah, Materials Science and Engineering Pan, Hongchao; University of Utah Bedrov, Dmitry ; University of Utah, Materials Science & Engineering

SCHOLARONE™
Manuscripts

Role of Cationic Group in Defining Structural and Dynamic Correlations in Anion Exchange Membrane: A Molecular Dynamics Simulation Study of Hydrated Quaternary Ammonium-functionalized Poly (p-phenylene oxide)-based Membrane

Received 00th January 20xx,
Accepted 00th January 20xx

DOI: 10.1039/x0xx00000x

www.rsc.org/

Dengpan Dong,[‡] Xiaoyu Wei,[‡] Justin B. Hooper^a, Hongchao Pan^a and Dmitry Bedrov^{*a}

Extensive atomistic molecular dynamics (MD) simulations employing polarizable force field have been conducted to study hydrated anion exchange membranes comprised of poly(p-phenylene oxide) (PPO) homopolymer functionalized with quaternary ammonium cationic side groups and hydroxide anion. Representative membranes with different cationic structures have been investigated to study correlations between polymer architecture, morphology and transport properties of hydrated membranes. Specifically, hydrated polymers with five different quaternary ammonium cationic groups (R_1 : $-\text{CH}_3$, R_2 : $-\text{C}_2\text{H}_5$, R_3 : $-\text{C}_3\text{H}_7$, R_4 : $-\text{C}_6\text{H}_{13}$ and R_5 : $-\text{C}_8\text{H}_{17}\text{OCH}_3$) and degree of functionalization of 50% were investigated at three hydration levels ($\lambda = N_{\text{water}}/N_{\text{cation}} = 5, 10$ and 17). Effects of polymer structure on distribution of water-rich domains and dynamic relaxations were systematically investigated to uncover a complex interplay between degree of hydrophobicity/hydrophilicity of cationic groups, morphology, connectivity of water domains, and transport mechanisms of hydroxide. Structural and dynamical analysis indicate that the bottlenecks, formed between the water-rich domains, create a substantial free energy barrier for hydroxide anion transport associated with the partial loss of its hydration structure. The energy penalty associated with the loss of the hydration structure hinders the vehicular transport of hydroxide anion. The optimal structure of functionalized homopolymer chains should be sufficiently hydrophobic to create nanophase segregation and form interconnected network of water channels with a minimal amount of narrow bottlenecks that inhibit vehicular motion of hydrated anions. We demonstrate that utilization of asymmetrically modified cationic groups is a promising route to achieve the desired water channel morphology at low hydration levels.

^a Department of Materials Science & Engineering, University of Utah, 122 South Central Campus Drive, Room 304, Salt Lake City, Utah 84112, United States

[†] Footnotes relating to the title and/or authors should appear here.

Electronic Supplementary Information (ESI) available: details of any supplementary information available should be included here. See DOI: 10.1039/x0xx00000x

[‡] Equally contributed as first authors.

1. Introduction

Due to the ability of direct conversion of chemical energy into electricity in an efficient and clean manner, fuel cells have attracted tremendous amount of interest in recent years, both from academic research and industrial applications.^{1,2,3,4,5} Despite the concept of fuel cells has been introduced in the 19th century, significant challenges are still present for all types of fuel cells, either due to economic concerns of precious metal used as the catalyst at electrodes or the degradation of fuel cell membrane materials during operation.⁶ The membrane, typically comprised of polymeric materials to provide an ion-conducting medium, is categorized to be either proton-exchange membranes (PEMs) or anion exchange membranes (AEMs). Compared to PEMs-based fuel cells, the operating temperature of alkaline fuel cells (AFCs) utilizing AEMs has to be lower due to chemical stability constraints, yet demonstrating that they can generate high voltages without using expensive platinum catalyst at the electrodes.^{7,8,9,10,11,12,13}

Initial design of AEMs was inspired by extensive studies of PEMs for which both theory and simulations provided valuable insight into microscopic correlations and phenomena.^{14,15,16,17} Although AEMs fuel cells are very promising in terms of clean, high efficiency in energy conversion, large challenges still exist in finding an optimal membrane design with high ion-conductivity, excellent mechanical properties, and desired chemical stability. This inspired a number of recent publications exploring a rational design specifically targeted for polymer-based AEMs.^{18,19,20,21,22,23,24,25} However, caution is needed when applying previous knowledge obtained from studying PEMs to the design of AEMs. For example, due to slower diffusion rate of hydroxide anions (OH⁻) compared to protons (H⁺), the polymer in AEMs often needs to have higher ion-exchange capacity (IEC) to achieve a comparable ionic conductivity. But the adverse effect associated with having high IEC is the high swelling of the membrane due to excessive water uptake, which leads to

displacement and Hofmann elimination effects by the OH⁻ anions.²⁶ To address this problem, research efforts are focusing on modification of side chains of the quaternary ammonium functional groups to hinder the attack from hydroxide as well as utilization of different cationic groups, such as e.g. imidazolium, phosphonium, ruthenium, etc..^{27,28,29} Based on the novel idea of designing AEMs with self-cross-linking and/or self-aggregating polymer backbones, Zhuang *et al.* systematically explored AEMs designs with various homopolymer architectures as well as different cationic groups. Their results showed drastic improvement on mechanical and chemical properties for AEMs with crosslinking when compared to non-crosslinking counterparts.^{30,31} However, despite great progress in search for promising candidates for AEMs, the fundamental correlations between polymer architecture and structural/dynamical properties of AEMs remain poorly understood. The design principles to systematically enhance the performance of AEMs are currently lacking due to the complexity of interplay between different structural and dynamic characteristics of AEMs and the diversity of possible polymer and functional group architectures.

Atomistic molecular dynamics (MD) simulation is a powerful tool that can provide detailed insight into atomic level interactions/correlations between different molecules/ions as well as their transport mechanisms. Using reactive force-field (ReaxFF) MD simulations, van Duin *et al.* studied the impact of water content on the structural and transport properties of three model AEMs with the poly(*p*-phenylene) oxide (PPO) backbone but different length of alkyl chains attached to the cationic side group (*i.e.*, PPO-trimethylamine, PPO-dimethylpropylamine and PPO-dimethylhexylamine).³² They found that increasing the alkyl chain length on the cationic side group protects the N⁺ from being attacked by OH⁻ ions, therefore improving the AEMs stability. In hydrated AEMs, the overall diffusion of OH⁻ has two primary contributions, the vehicular mechanism, when the hydroxide anion diffuses

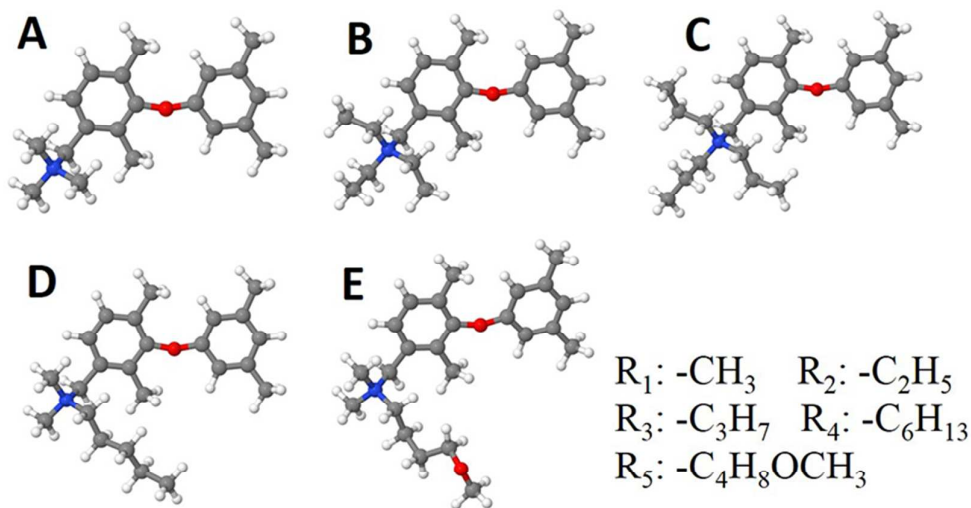


Figure 1. Structure of PPO-AEMs monomers with cationic functional groups (A) 3R₁; (B) 3R₂; (C) 3R₃; (D) 2R₁R₄; (E) 2R₁R₅. Color scheme: carbon atoms are grey, nitrogen atoms are blue, oxygen atoms are red, and hydrogen atoms are white.

reduced mechanical integrity of AEMs.²⁴ Another concern is the relatively low chemical stability of the quaternary ammonium functional groups, which is originated from nucleophilic

through the surrounding environment following the fluctuations and gradients in concentration and electrochemical potential, and the Grotthuss mechanism, when proton hops from

surrounding water to OH^- , therefore converting proton donating water molecule into hydroxide.^{13,33,34} Recently Chen *et al.* investigated the OH^- solvation structure and its transport mechanisms in poly(vinyl benzyltrimethylammonium) using a multiscale reactive MD simulation method.³⁵ In that work, the evenly-distributed cationic side groups along the polymer backbone helped to generate a continuous domain of overlapping regions of the first hydration shells of the cationic groups, which facilitated the overall transport of OH^- via both vehicular and Grotthuss mechanisms. They also found that compared to the PEMs, AEMs have a more localized excess charge solvation structure, where the free energy barrier between “hopping states” is higher, and as a result, the vehicular mechanism contributed more to the OH^- transport than the Grotthuss mechanism. However, the latter conclusion is at odds with the findings that proton transport should be facilitated in narrow water channels.^{36,37} Another recent MD simulation study that utilized combined reactive and non-reactive force fields demonstrated the importance of the Grotthuss mechanism in facilitating transport of OH^- through bottlenecks in narrow water channels forming in AEMs at low water uptakes.³⁸

Despite the important insights provided by simulation works mentioned above, there are numerous issues related to the coupling of structural and dynamic properties that remain poorly understood. Therefore, in this work, we have conducted systematic investigation of the influence of cationic side group structure on the underlying nanoscale structure, water distribution and the effect of these structural features on the vehicular motion of hydroxide anion. In our simulations, we utilized classical MD simulations based on Atomistic Polarizable Potential for Liquids, Electrolytes, and Polymers (APPLE&P) force field,³⁹ that have been successfully applied to a wide variety of materials (*e.g.*, ionic liquids,⁴⁰ electrolytes,^{41,42} polymers,⁴³ and liquid crystals⁴⁴). While these simulations do not provide sampling of the Grotthuss mechanism directly, they do allow us to study correlations between the nanoscale structure of water domains and vehicular transport of hydroxide ions and to make important conclusions regarding Grotthuss mechanism contribution based on the estimated ionic conductivities. Specifically, we investigated membranes comprised of poly(2,6-dimethyl-1,4-phenylene oxide) (PPO) based polymers functionalized with quaternary ammonium side groups. Membranes comprised of this homopolymer showed reasonably high mechanical, chemical, thermal and hydrolytic stability in alkaline conditions. PPO-based AEMs are also easy to synthesize and process. We investigated PPO chains functionalized with five different cationic groups as illustrated in Figure 1. These polymer chains were investigated at hydration levels (defined as the ration of number of water molecules to number of cationic groups) $\lambda = 5, 10$, and some at 17, which spans the typical hydration levels for promising membranes of this type.⁴⁵

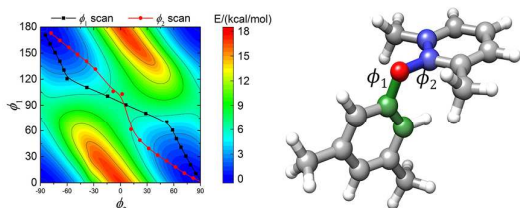


Figure 2. Conformational energy scan for the PPO dimer as a function of ϕ_1 and ϕ_2 . Contour map shows conformational energies from the force field, red and black symbol lines show ϕ_1 and ϕ_2 scan paths from DFT calculations.

2. Simulation Details

2.1 Force field development

To study these systems we used a polarizable model which is based on the APPLE&P force field coupled with the SWM4-AD water model.⁴³ The repulsion dispersion parameters, partial atomic charges, and isotropic polarizabilities for polymer atoms were directly transferred from the APPLE&P as they were previously parameterized and validated for related compounds including alkyl ammonium cations and organic molecules with benzene rings.^{44,46} The validation and transferability of the force field for cationic alkyl ammonium side groups, especially the van der Waals interaction with water, were verified in our recent simulation study.⁴⁷ The oxygen atom in PPO segment is involved in two key dihedrals ϕ_1 and ϕ_2 highlighted in Figure 2. These two dihedrals essentially define the chain conformational flexibility and mobility. The total conformational energy scan with respect to ϕ_1 and ϕ_2 , obtained from our force field for PPO dimer is presented in Figure 2. The contour plot shows two deep energy maxima that correspond to conformations in which the two benzene rings are parallel to each other. Two dihedral drives have been sampled by DFT calculations for the PPO dimer using Gaussian09 software at B3LYP theory combined with 6-311G(++) basis set.^{48,49} In the first path, starting from a global minimum energy geometry ϕ_1 was changed in small increments while all other degrees of freedom were allowed to relax (including the angle ϕ_2). The resulting path is shown in Figure 2. In the second path, we changed ϕ_2 and let the other degrees of freedom to relax. While the second path had a different trajectory, both paths went through the same saddle point with the relative energy of 6.5 kcal/mol. The force field parameters for both dihedrals were adjusted to provide an accurate description of both paths. As can be seen from Figure 2, the location of the saddle point predicted by DFT paths is consistent with the energy profiles obtained from our force field, while the 6.6 kcal/mol energy at the saddle point predicted by the force field is in excellent agreement with the DFT predictions.

Table 1. Self-diffusion coefficient of hydroxide in bulk water obtained from simulations using different models.

	APPLE&P	CRM ⁵⁰	MS-EVB ⁵¹	LEWIS ⁵²	EXP ⁵³
D (10^{-9} m ² /s)	1.9	1.7	2.2	1.5	5.03

The force field for hydroxide anion was parameterized based on DFT benchmark energies and geometry structure for a cluster containing one OH^- and five neighboring water molecules, shown in Figure S1 in the Supplementary Information (SI). The geometry of this cluster was optimized using quantum chemistry package Gaussian09, utilizing M052X level of theory and aug-cc-pVDZ basis set.^{54, 55} The repulsion/dispersion parameters for anion-water interactions were adjusted to yield the same binding energy for the cluster as calculated from quantum chemistry (cluster configuration was kept at the minimal energy geometry predicted by quantum chemistry calculation).

The ability of our polarizable hydroxide force field to capture dynamical properties was tested by conducting simulation of a reference system, where one TMA/ OH^- pair is dissolved in 500 water molecules. At 298 K, the self-diffusion coefficient of hydroxide (D_{OH^-}) was calculated and compared with predictions

from MD simulations using other hydroxide models and experimental data as shown in

Table 1. The D_{OH^-} calculated from MD simulation utilizing our force field was $1.9 \times 10^{-9} \text{ m}^2/\text{s}$, which is comparable with $1.7 \times 10^{-9} \text{ m}^2/\text{s}$ predicted by a more complex and advanced charged ring model (CRM).⁵⁰ The experimental value of $5.03 \times 10^{-9} \text{ m}^2/\text{s}$ ⁵³ is noticeably larger than predictions from our classical simulations, which is expected as the D_{OH^-} from our simulations does not include the Grotthuss mechanism which can substantially increase the effective OH^- transport rate. Note that MS-EVB model⁵¹ that explicitly includes the Grotthuss transport predicts a similar value of $2.2 \times 10^{-9} \text{ m}^2/\text{s}$ for diffusion of hydroxide in water. The underestimation of D_{OH^-} from this reactive model can be attributed to the absence of nuclear quantum effects, causing the overestimation of the transitional barrier for proton hopping.^{35,56}

2.2 System setup and simulation protocol

Each system contained 16 identical polymer chains comprised of five repeating units (see Fig 1). The degree of functionalization of chains in all systems was 50% with alternating order of functionalized and unmodified phenylene units. Simulations of the $3R_1$ polymer were conducted at three hydration levels ($\lambda=5, 10$ and 17 , which corresponds to 400, 800, and 1360 water molecules, respectively), while simulations of all other systems were done at $\lambda=5$ and 10 . Electrostatic interactions were calculated using the Ewald summation. The cut-off radius for calculation of van der Waals interactions and the real part of Ewald summation was 15 \AA . The induced polarization at each atom was calculated iteratively by minimizing the total electrostatic energy with respect to the electrostatic field induced by neighbouring point charges and dipoles. The Thole screening was utilized to avoid the 'polarizability catastrophe'.⁵⁷ All bond lengths were constrained by using the SHAKE algorithm.⁵⁸ The integration of equations of motions was performed using the multiple time step method with 0.5 fs time step used for valence interactions, including bonds, bends, and out-of-plane bending, 1.5 fs integration step for dihedrals and the short-range (less than 8 \AA) non-bonded interactions, and 3.0 fs integration step for the remaining non-bonded interactions within 15 \AA truncation distance and the reciprocal part of Ewald summation.

To prepare the systems, initially polymer chains, hydroxide anions, and water molecules were randomly placed inside a large simulation cell (side length of 300 \AA). The system was

shrunk to a reasonable density over 2 ns run at 298 K followed by simulation in the NPT ensemble until the cell dimensions have stabilized. The system was then heated up to 2000 K in the NVT ensemble and run at this elevated temperature for 3 ns to allow relaxations of polymer chain conformations at the desired density. Finally, each system was annealed to 298 K over 3 ns run and subsequently run in the NPT ensemble for 5 ns to reach a steady state. After such preparation, production runs were conducted in the NPT ensemble for more than 30 ns .

3. Results and Discussion

3.1 Structural properties

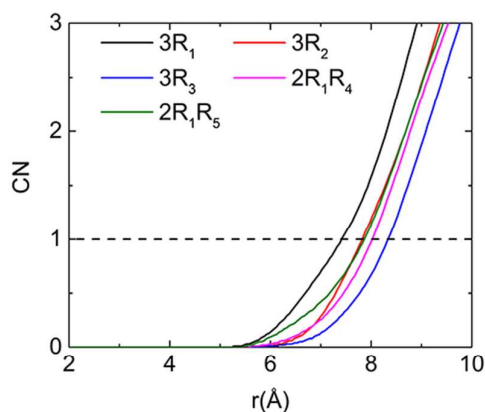


Figure 3. The N^+-N^+ coordination number obtained from MD

We begin characterization of the modelled membranes with examination of several key pair correlation functions that define the distribution of ions and water as well as local coordination of ions.

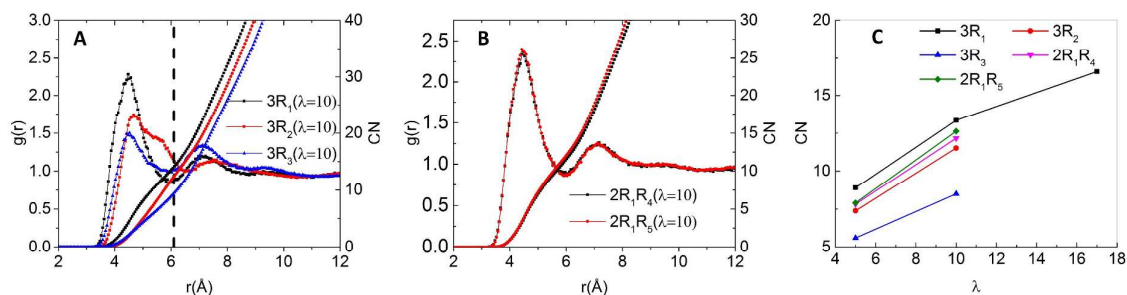


Figure 4. N^+-O_w correlation at hydration level $\lambda=10$ (A, B) and coordination number of water around N^+ within first coordination shell (C) defined as a sphere with 6.1 \AA in radius.

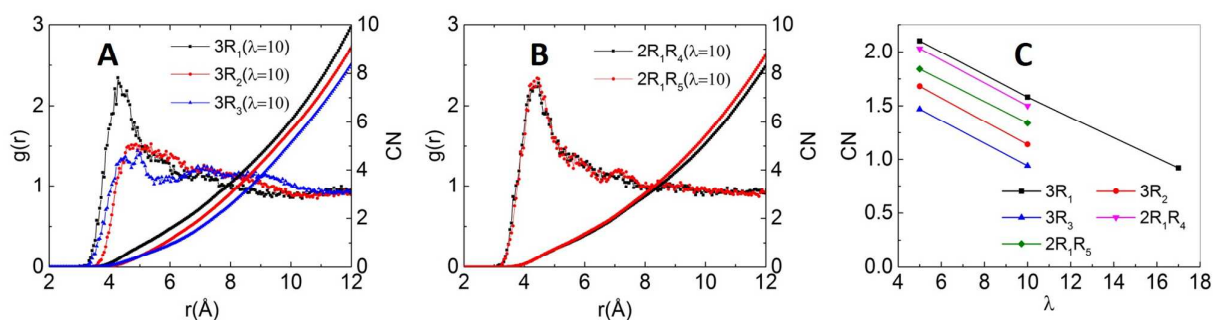


Figure 5. $N^+-O_{OH^-}$ RDFs at hydration level $\lambda=10$ (A, B) and coordination number of OH within the first hydration shell (C).

N^+-N^+ pair correlation. The correlation between cationic nitrogen (N^+) groups is one of the main structural characteristics of these membranes as the N^+ groups are predominantly distributed at the interface between polymer and water rich domains, and play a key role in defining transport of hydroxide anions. However, examination of the N^+-N^+ radial distribution functions (RDF) $g(r)$ is not the most informative for this purpose, due to its inability to distinguish whether a certain pair is separated by the water or polymer phase. The $g(r)$ for N^+-N^+ correlations in all systems are shown in Figure S2 of the SI. Here, we only would like to focus on the corresponding coordination number (CN) as a function of separation (or within a sphere of radius) from a N^+ atom. Figure 3 shows the apparent CN for all investigated systems at hydration level $\lambda=10$. The plot indicates that within 7–8 Å there is on average one other N^+ group in the system. Therefore, this can be one of the key characteristic length scales that hydroxide ion would have to deal with if its motion is defined by moving from one cationic group to another. At CN=1, the $3R_1$ system has the shortest separation (7.3 Å) between the nearest neighbours, while in much bulkier $3R_3$ groups, the CN=1 is reached within 8.2 Å distance. All other systems show correlations in-between of those two limiting cases. Note that in all systems no N^+ come closer to each other than 5.2 Å.

N^+-O_w pair correlation. The $g(r)$ for the N^+-O_w correlation is more informative in revealing the hydration structure around cationic nitrogen as shown in Figures 4 A and B for $\lambda=10$. In all systems, there is a well-defined first peak in RDF that is located

around 4.5 Å. The secondary peak in N^+-O_w correlation is observed between 7 and 8 Å. For all polymers, the locations of the first minima at 6.1 Å of $g(r)$ can be used to define the first coordination shell, illustrated in Figure 4 A by the vertical dashed line. The corresponding CNs in the first hydration shell are shown in Figure 4 C as a function of hydration level. In the case of symmetrically modified cationic groups ($3R_1$, $3R_2$, $3R_3$) at $\lambda=5$, the total number of water molecules in the first hydration shell varies from 5.6 ($3R_3$) to 8.9 ($3R_1$), as shown in Figure S3 A. At $\lambda=10$, these values increase to 8.5 and 13.3, respectively. As the length of alkyl tail increases, the RDF peak becomes broader and shifts to larger distance. This feature is consistent with experimental study revealing enhanced hydrophilicity going from tetra-methyl ammonium to tetra-ethyl ammonium.⁵⁹ Figure 4 B shows that the asymmetrically modified polymers ($2R_1R_4$ and $2R_1R_5$) yield almost the same N^+-O_w correlations as in $3R_1$ although the corresponding CN is slightly lower as shown in Figure 4 C. Despite being comparable to the $3R_3$ in size of alkyl group (*i.e.*, having similar number of heavy atoms), the $2R_1R_4$ and $2R_1R_5$ have noticeably more water molecules surrounding each cationic nitrogen. The number of water molecules in the first shell of $2R_1R_4$ and $2R_1R_5$ are comparable at $\lambda=5$, while more water molecules are surrounding the cationic N^+ in $2R_1R_5$ in the first shell at $\lambda=10$.

$N^+-O_{OH^-}$ correlation. The cation-anion correlations are shown in Figure 5 A and B. In the case of $3R_1$, a well-defined peak in $N^+-O_{OH^-}$ $g(r)$ is located at 4.4 Å. For symmetric cationic groups with longer alkyl chains ($3R_2$ and $3R_3$), the featured N^+-

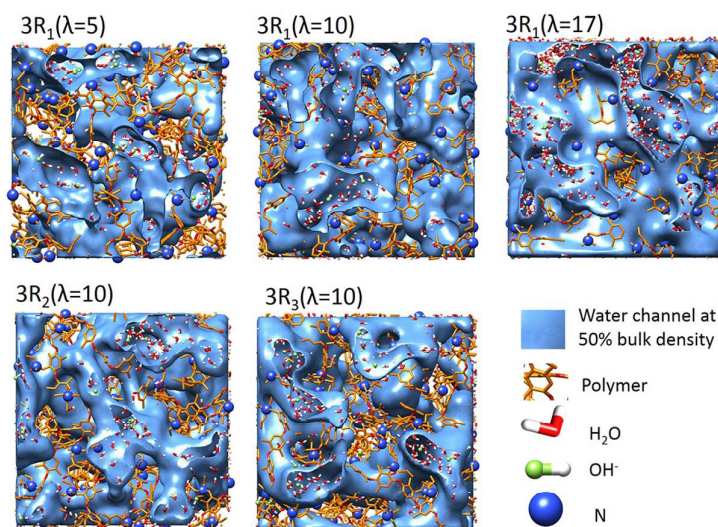


Figure 6. Snapshots of membrane structure with highlighted water domains. Water channels are defined by isosurfaces of local water density at 50% of bulk water density.

O_{OH} correlation is diminished and does not show any well-defined peaks due to steric effects induced by alkyl groups. On the other hand, for $2R_1R_4$ and $2R_1R_5$ the first peak is very similar to what is observed in $3R_1$ (Figure 5 B), indicating that a single long tether (R_4 or R_5) is not sufficient to preclude direct interaction between the core of the cationic group and the hydroxide. The corresponding CN of OH^- in the first hydration shell is given in Figure 5 C. For both symmetric and asymmetric functionalization groups, the CN of OH^- decreases with increasing of hydration level, meaning that more OH^- become free anions solvated by water at higher hydration levels. At $\lambda=5$, the number of OH^- in the first hydration shell of N^+ was calculated to be 2.1, 1.7 and 1.5 for $3R_1$, $3R_2$ and $3R_3$, respectively, while at $\lambda=10$ the corresponding CN of OH^- decreased to 1.6, 1.1 and 0.9. In the cases of polymers with asymmetric functional groups, the CN of $2R_1R_4$ is very similar to coordination in $3R_1$ system, while for $2R_1R_5$ CN is somewhat lower, indicating that for these groups bonding to the cationic nitrogen N^+ is still accessible to hydroxide.

Morphology of water channels. Understanding the correlations between polymer structure and morphology of water channels as well as the transport of ions through those channels is crucial in designing novel membranes with desired conductivity. Snapshots of typical structures of water channels observed in investigated systems are shown in Figure 6. Isosurfaces of local water density corresponding to 50% of bulk water density are shown as solid surfaces. The isosurfaces were generated using the Chimera software⁶⁰ by calculating the local water density on the grid and saving it in the Gaussian cube file format. Due to nano-scale phase separation, the systems with symmetrically modified cationic groups show well-defined water channels. However, those channels are inhomogeneous, showing prominent variance in the channel dimensions at different locations. Typically, a percolating network of nanoscale water domains can be observed. The size of water channels increases dramatically with increasing hydration level.

As the length of alkyl tails on symmetrically modified cation group, *e.g.* $3R_3$, increases the phase segregation between polymer and water is further enhanced, causing the formation of larger water channels with reduced connection between those domains even at $\lambda=10$. However, in the $3R_2$ system, the nano-phase segregation is reduced compared to $3R_1$, which coincides with the conclusion that TEA^+ being more hydrophilic than TMA^+ ⁵⁹ and a recent study that introducing hydrophilic group leads to improvement of continuation of water channel in AEMs.⁶¹ The structure of water channels in systems with asymmetric cationic groups is shown in Figure S4. These systems feature morphological characteristics as observed in $3R_1$ and $3R_3$ systems. Comparable water channels were observed in $2R_1R_4$ and $2R_1R_5$, indicating that introduction of ether oxygen in hexyl group did not change hydrophobicity significantly, as will be discussed below in the analysis of channel size distributions and self-diffusion coefficients.

From the analysis of the N^+-N^+ correlation we found that the increase of side chains length leads to a larger separation between cationic groups in the system. However, the size of water channels does not necessarily follow the same trend, which makes it difficult to interpret the structure of nanophase separated water channels based on N^+-N^+ or N^+-O_w correlations alone. Figure 6 suggests that the structure of water channels has prominent heterogeneity and therefore cannot be characterized by the averaged correlation analysis of RDFs.

Size distribution of water channels. The most straightforward method to characterize the morphology of water channels is to directly analyze the distribution of channel sizes, which can be achieved by calculating the pore size distribution (PSD).⁶² Following the approach illustrated in the chart flow in Figure S5, we have calculated the distribution of cross-sectional dimensions of “pores” in the polymer matrix occupied by water. The PSD of $3R_1$ at different hydration levels is shown in Figure 7 A. At $\lambda=5$, for $3R_1$ polymer, the smaller diameter water channels are observed with the most probable size of about 5 Å. The most probable size increases to 7 Å with increasing of hydration level to $\lambda=17$, and shows broader distribution. In the $3R_3$ system at $\lambda=5$, a broader distribution with dimensions of water channels extending to 10 Å is seen in the PSD pattern, which is consistent with the stronger nano-scale segregation observed in Figure 6 for this system. However, in this system the water domains appear to be more isolated, *i.e.*, have fewer connections between them, reflected by extension of the distribution to the region of smaller channel

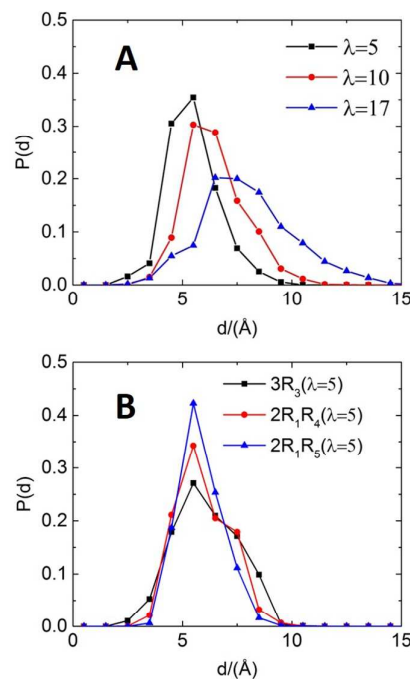


Figure 7. Distribution of water channel size: (A) $3R_1$ at various hydration level and (B) different functional groups at $\lambda=5$.

sizes (less than 4 Å), especially at $\lambda=10$ as shown in Figure S6 A.

Compared to $3R_3$ at $\lambda=5$, a narrower distribution of channel sizes was observed in the $2R_1R_4$ and $2R_1R_5$, as illustrated in Figure 7 B. Due to further enhancement in the strength of hydrophilicity for $2R_1R_5$, the size of water channels is remarkably more uniform than in $2R_1R_4$. At $\lambda=10$, shown in Figure S6 B, combined features from $3R_3$ and $3R_1$ can be observed in distributions for $2R_1R_4$ and $2R_1R_5$. In the case of $2R_1R_5$, the introduction of hydrophilic ether group enhances the interaction between the long alkyl chain and water, and consequently, leads to a reduced phase separation at $\lambda=5$. Therefore, compared to $2R_1R_4$, $2R_1R_5$ shows more probability for smaller pore sizes and

the formation of narrow connections in the water channel, as shown in Figure 7 B.

From the above analysis, it is rational to describe the water phase structure as a combination of large water-rich domains and smaller 'interconnections' between them. From the view point of optimizing the overall hydroxide mobility inside water channels, on the one hand, the nano-phase separated structure with high probability of larger water channels is desirable. On the other hand, maintaining the essential interconnections between these water domains (*i.e.*, avoiding the formation of bottleneck-like connections) is also indispensable. The $3R_1$, $2R_1R_4$ and $2R_1R_5$ appear to be good candidates which meet the above requirements. The $3R_3$, in which noticeable bottleneck-like connections can be observed, seems to provide the worst morphology of water-rich domains for anion transport. In the next section, we will analyze the dynamical properties of investigated membranes and attempt to correlate the observed trends in dynamics with the underlying membrane structure.

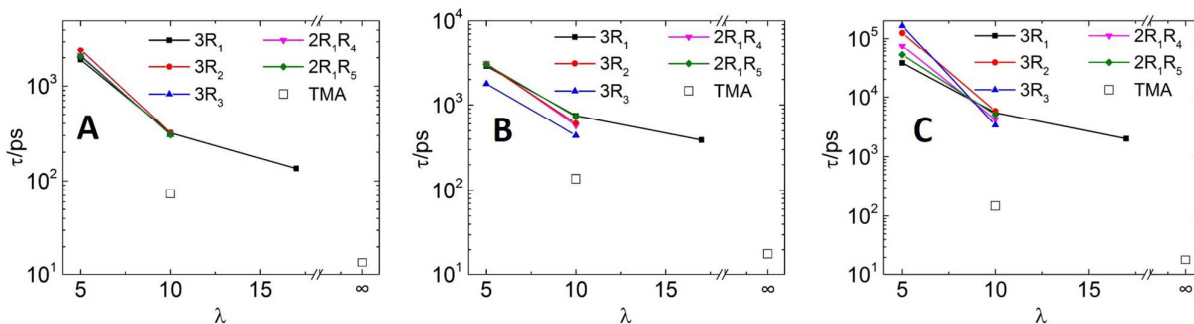


Figure 8. Characteristic residence time of water inside the first hydration shell of hydroxide (A), cationic hydration shell (B) and OH^- inside the first hydration shell of cation (C).

3.2. Dynamical properties

Residence times. One of the key characteristics of the charge transport properties is the residence time, τ , defined as the time one specie spends near the other. Specifically, in investigating AEMs the interest is in the residence times of water and anion near the cationic group as well as water around anion. Using the RDFs, we have defined the first coordination shell of N^+ as 6.1 Å for water and OH^- . The first coordination shell of OH^- by water was defined as 3.4 Å. Then the residence time of these molecules in the vicinity of cation/anion group can be obtained by examining the autocorrelation function (ACF):

$$ACF(t) = \frac{\langle H_{ij}(t)H_{ij}(0) \rangle}{\langle H_{ij}(t) \rangle \langle H_{ij}(0) \rangle} \quad (1)$$

where $H_{ij}(t) = 1$, when water or OH^- are inside the defined coordination shell, otherwise $H_{ij}(t) = 0$. The $\langle \rangle$ denotes the ensemble average. The ACF decays to zero after coordination of all N^+ cationic groups (or OH^-) has changed compared to that at time zero (*i.e.*, all molecules present in the hydration shell at time zero were replaced with new molecules). The ACF function can be fitted by the Kohlrausch-Williams-Watts (KWW) function⁶³

$$P(t) = A \exp \left[- \left(\frac{t}{\tau_{KWW}} \right)^\beta \right] \quad (2)$$

and the characteristic residence time can be obtained by integrating the KWW fit:

$$\tau = \int_0^\infty P(t) dt \quad (3)$$

The characteristic residence times of water molecules inside the first coordination shell of anion and cation hydration shells are shown in Figure 8 A. For the reference, in the TMA⁺/OH⁻/water system at 298 K where one TMA/OH⁻ pair was dissolved in 500 H₂O (*i.e.* $\lambda=500$), $\tau_{OH^- - O_w}$, $\tau_{N^+ - O_w}$, and $\tau_{N^+ - OH^-}$ have been calculated to be 12.6 ps, 5.3 ps and 8.9 ps in a previous study using MS-EVB model,⁶⁴ which is comparable to the bulk water system in this study, *i.e.* 13.5 ps, 16.3 ps and 17.8 ps. For $\tau_{N^+ - O_w}$, the result of this study is more consistent with simulation predictions using non-reactive force field that found $\tau_{N^+ - O_w} = 18.0$ ps.⁶⁵ In the polymer systems, the $\tau_{OH^- - O_w}$ decreases with increasing hydration level. At low hydration level ($\lambda=5$) the water residence time near anionic groups is ranging between 1.9 and 2.4 ns depending on the system. Surprisingly, at a given hydration level, similar $\tau_{OH^- - O_w}$ were observed for all

systems despite the manifested difference in the structure of polymer membrane. As the hydration level increases from $\lambda=5$ to $\lambda=10$, the characteristic residence time of water near OH^- drops and becomes almost independent of chemical structure of the cationic group (varies in the narrow range between 305 ps and 320 ps). These residence times can be compared to the residence times of water near anion in the TMA/OH⁻/water mixtures. As the hydration level further increases, the influence on the water residence time becomes weaker as can be observed for $3R_1$ in which at $\lambda=17$ the residence time is levelling at about 135.0 ps.

Similar concentration dependence is observed for the residence time of water near cationic groups. However, unlike the residence near anion, the effect of chemical structure of cationic tethers is prominent both at $\lambda=5$ and 10. At low hydration level, the $\tau_{N^+ - O_w}$ in $3R_3$ is significantly lower than all the other systems that yield comparable $\tau_{N^+ - O_w}$. The dependence of $\tau_{N^+ - O_w}$ at $\lambda=10$ follows the hydrophobicity strength of the side chains as well as the size of local water domains. Consistent with the channel size distribution presented in Figure 7, the $\tau_{N^+ - O_w}$ is significantly reduced for $3R_3$, due to enhanced hydrophobicity and sterically more crowded hydration shell that does not allow water molecules to develop hydrogen bonding network. The $\tau_{N^+ - O_w}$ follows the order: $2R_1R_5 \approx 3R_1 > 2R_1R_4 \approx 3R_2 > 3R_3$, and it spans the range between 439.0 ps and 745.6 ps. The $\tau_{N^+ - O_w}$ in TMA/OH⁻/water reference system is calculated to be 137.0 ps at $\lambda=10$.

Finally, the $\tau_{N^+-OH^-}$ residence time, which most directly impacts AEM charge transport efficiency, is presented in Figure 8 C. At $\lambda=5$, consistent with the relatively disconnected network of water channels, the residence of OH^- around N^+ shows a long-living feature and the estimated residence times are on the order of hundreds of nanoseconds. At $\lambda=10$, the dependence of $\tau_{N^+-OH^-}$ on cationic group structure shows the trend similar to $\tau_{N^+-O_w}$, i.e., $2R_1R_5 \approx 3R_1 > 2R_1R_4 > 3R_3$. However, the residence time values are almost an order of magnitude longer than those observed for water.

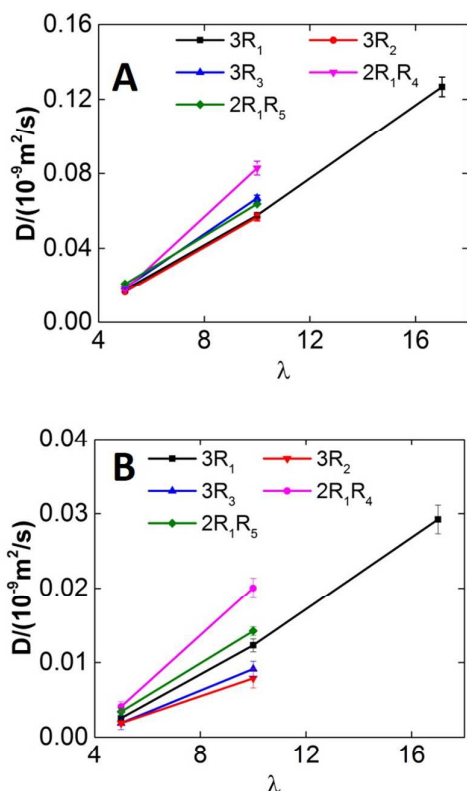


Figure 9. Self-diffusion coefficients of (A) water and (B) OH^- inside water channels.

Diffusion of OH^- and water. Next, diffusive characteristics of OH^- and water molecules inside the water channels are analysed. Figure 9 shows the self-diffusion coefficient of water, D_{H_2O} , and hydroxide, D_{OH^-} , that were calculated via the Einstein relation:

$$D = \lim_{t \rightarrow \infty} \frac{\langle MSD(t) \rangle}{6t} \quad (4)$$

where $MSD(t)$ is the mean-square displacement of the center of mass of considered molecules over time t and $\langle \rangle$ denotes an ensemble average. The D_{H_2O} and D_{OH^-} were obtained by fitting the long-time slope of $MSD(t)$ in the diffusive regime and are shown in Figure 9 A and B, respectively. While the effect of the cationic group chemical structure on D_{H_2O} is not pronounced, the concentration dependence of D_{OH^-} is quite pronounced showing a factor of 3-4 increase upon increasing the hydration level from $\lambda=5$ to $\lambda=10$. Figure S10 in the SI further illustrates this

concentration dependence coefficients by comparing the ratio of water and hydroxide self-diffusion coefficients.

Non-Gaussianity parameter. Calculation of the non-Gaussianity parameter $\alpha_2 = \frac{3\langle r^4(t) \rangle}{5\langle r^2(t) \rangle^2} - 1$ allows one to analyze the heterogeneity of water and anion dynamics.⁶⁶ This parameter is shown in Figure 10 as well as Figures S7-9 in SI. In all cases, the non-Gaussianity parameter exhibits a well-defined peak at short time scale of around 15 ps, which can be attributed to the time scale defining the local motion in the water-rich domains and interaction with neighboring molecules. For water we observe a single peak in α_2 after which the non-Gaussianity parameter is monotonically decreasing with respect to time.

For anion, a more complex behaviour of α_2 is observed, where in addition to the α_2 peak at around 20 ps, there is a clear indication of a second peak or a shoulder at time scales between 1-10 ns. There are several length scales and associated diffusion processes that can be contributing to increased dynamical heterogeneity of anion on different time scales. On the short time and length scales, the dynamic heterogeneity is determined by relaxation of the local cage environment, e.g. N^+-O_w , N^+-OH^- and OH^-O_w correlations. Since the anion movement is primarily correlated with the motion of water, this time scale is very similar to what is observed for dynamic heterogeneity of water molecules, yielding the featured α_2 peak at around 20 ps. On intermediate length scales, the mobility of anion is determined by whether it is associated with a cationic group (i.e., located in the first coordination shell) or surrounded by water. The time scale relevant to define this dynamic heterogeneity will be comparable to the residence time of anion near cation and the time scale it takes for anion to diffuse from one cationic group to another. Finally, due to very heterogeneous morphology of the water-rich domains and the presence of 'bottlenecks' between them, another source for dynamic heterogeneity, showing up on much longer time and

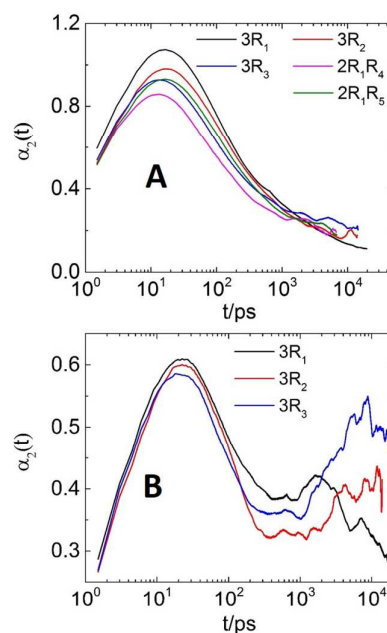


Figure 10. Non-Gaussianity parameter at hydration level $\lambda=10$ for dynamics of (A) water, (B) OH^- in symmetrically modified cationic groups.

length scales, corresponds to anion diffusion between different water domains.

Taking into account that investigated polymers have a relatively high glass transition temperature, we can expect that the first two processes are related to the activation energy associated with escaping the local environment (and hence will be sensitive to the temperature) while the last process is primarily sensitive to the underlying membrane morphology, which would not change much if we take an already equilibrated system and just raise the temperature such that the polymer membrane does not undergo any significant structural changes. To justify the attribution of the second peak in the non-Gaussianity parameter to the diffusion through inter-domain bottlenecks, the α_2 was analysed as a function of temperature and is presented in Figure S7.³⁵ The same $3R_1$ system at $\lambda=10$, was studied at 298 K, 323 K and 353 K. From the time dependence of α_2 , the relaxation of heterogeneity in dynamics of OH^- and water shifted to the shorter times. However, the spatial scale showed trivial temperature dependence, showing the identical location for the peaks in α_2 . We also want to point out that in terms of diffusion through the 'bottleneck', OH^- anions experience significant loss of coordinating H_2O (losing about 2 H_2O molecules). When H_2O molecule transitions through the same bottlenecks it requires smaller rearrangement of its coordination shell. Also waters coordinating the OH^- which is near the bottleneck can leave the OH^- hydration shell (i.e. are replaced by other water molecules) and diffuse through the bottleneck. Therefore, even the water molecules near OH^- would likely to have a different heterogeneity and sensitivity to the bottleneck structure/distribution than hydroxides. The difference in the behaviour of H_2O when diffusing through a bottleneck can be seen in Figure S12. Therefore, the non-Gaussianity parameter for water molecules does not manifest the same features observed for OH^- at longer time and length scales.

Considering the averaged distance between neighboring N^+ ranges between 6.3 Å ($3R_1$) and 8.2 Å ($3R_3$) and the range of the first cationic hydration shell from 3.5 Å to 6.1 Å, the size of overlapped water domains is estimated to be 3-4 Å. Nevertheless, the second peak in α_2 peak is located between 7 and 14 Å, as observed in α_2 -MSD correlation shown in Figure S7 C and D, which validates previous attribution of the second α_2 peak to the diffusion through inter-domain bottlenecks. The timescale of the second α_2 peak reflects the transport efficiency of water channel, i.e., the shorter the time scale the shorter time is required to diffuse through the 'bottlenecks' of water channels. From estimated PSD, shown in Figure S6, lower probability for smaller channel sizes and slightly higher probability for larger channel sizes was identified in $2R_1R_4$ compared to $2R_1R_5$. Consequently, the timescale for the featured non-Gaussianity peak is reduced in $2R_1R_4$ indicating a shorter time required for the diffusion through the water channel 'bottleneck' and therefore leading to a 40% increase in diffusion coefficient of OH^- in $2R_1R_4$ compared to $2R_1R_5$.

Correlation of D_{OH^-} with bottleneck distribution. To quantify the correlation between D_{OH^-} and the distribution of water channel bottlenecks, we calculated the volume fraction of such bottlenecks in the formed channels. We defined a bottleneck region as a portion of the water channel which can accommodate spheres with radius less than 2.4 Å (big enough to fit OH^- - H_2O pair) and larger than 1.5 Å (accommodate a single OH^-). The accumulated volume of these domains normalized by the total volume of water channels is a quantitative measure of

the volume fraction of bottlenecks. At $\lambda=10$, the correlation

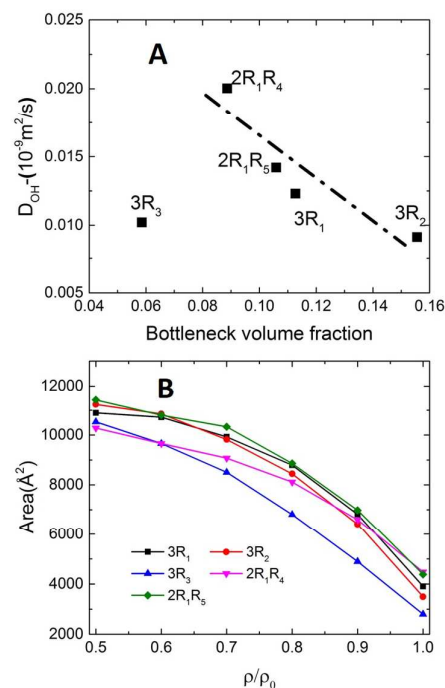


Figure 11. D_{OH^-} as a function of bottleneck volume fraction (A) and total surface area of the water channels as function of isosurface density value used for defining water channels (B).

between D_{OH^-} and the volume fraction of bottlenecks is shown in Figure 11 A. Except for the point at 0.059, which corresponds to $3R_3$, D_{OH^-} increases with decreasing volume fraction of bottleneck regions. Consistent with enhanced phase segregation observed in the $3R_3$ systems, the surface area of water channels defined by isosurfaces with ρ/ρ_0 larger than 0.5 (i.e. larger than 50% of bulk density) is shown in Figure 11 B. For any value defining the isosurface, the $3R_3$ system has the smallest surface area, indicating the formation of large water-rich domains and limited interconnection between them. Therefore, the slow dynamics in the $3R_3$ with low volume fraction of bottlenecks, can be attributed to the disconnect of water domains and leading to OH^- transport from one water-rich domain to a neighboring one to be hindered.

4. Discussion and Concluding Remarks

Channel size heterogeneity: impact of bottlenecks. In the water-rich domains, the anion-water cluster can move freely without destroying the structure of the cluster, however, the mobility of the cluster will be severely retarded when migrating through the bottlenecks in the water channel. Figure 12 shows a typical process of OH^- /water cluster (in $2R_1R_4$ at $\lambda=10$) migrating through the water channel bottleneck, which required about 6 ns. At time $t=0$, we have selected an anion and its neighboring water molecules within the first hydration shell (highlighted as green and red spheres, respectively, in Figure 12). Snapshots show the location of labelled molecules at $t=0, 2, 5, 6.2$ and 7 ns. The initial cluster was stable for about 5 ns, showing small displacement from its original location at $t=0$ and oscillations in OH^- coordination number. At $t=4.7$ ns a noticeable decrease (to

as a low as 2) in the total number of coordinating water molecules was observed, implying a disruption of the coordinating environment. Following this disruption, a diffusion 'jump' of OH⁻ was observed, leading to a 6-Å displacement within 200 ps. The overall coordination of OH⁻ by water was restored after this 'jump' into another water-rich domain but

hydroxide in our systems is almost an order of magnitude lower than experimental data for AEMs with similar structure, degree of functionalization, and hydration levels.⁶⁸ This implies that the Grotthuss mechanism must play a much more significant role than what has been considered before. Indeed, our recent simulation study using combined APPLE&P and ReaxFF force

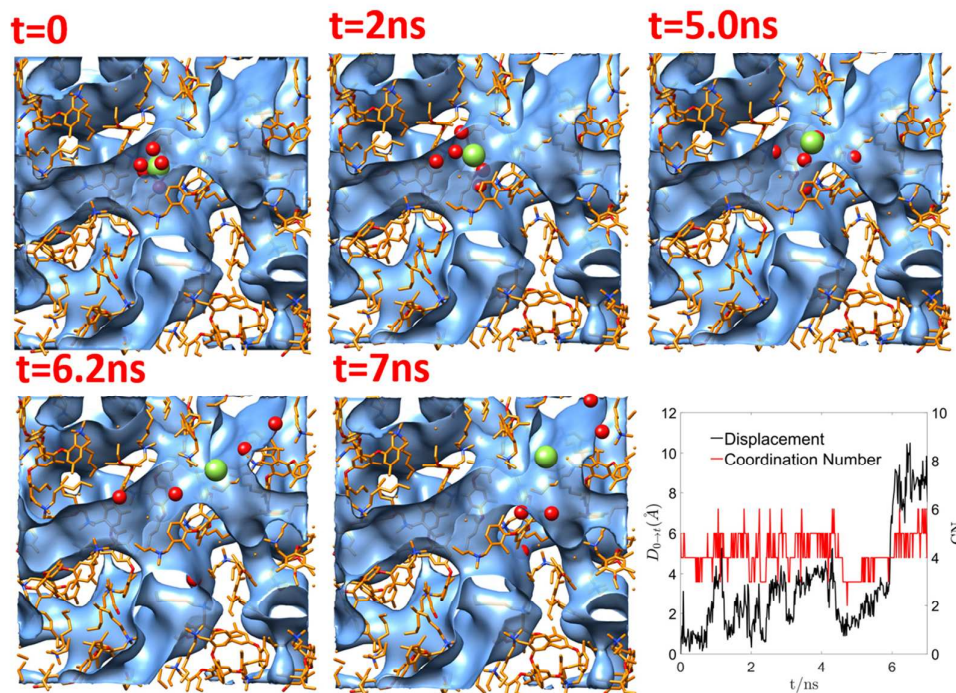


Figure 12. Illustration of dissociation of an anion-water cluster when crossing a 'bottle-neck' in the water channel. Graph shows time evolution of displacement and coordination number of water molecules for the selected hydroxide anion.

the coordination shell was now comprised of a completely new set of water molecules. Clearly, such transitions through bottlenecks that require anion to lose part of its hydration shell have to have higher free energy barriers and therefore create additional resistance for the ion transport.

As discussed above, simulations of hydroxide anion in dilute aqueous solution showed that our force field capture the vehicular mobility very well compared to what is predicted from ab initio MD or models that include the Grotthuss mechanism explicitly. Also, our simulations of tetraalkyl ammonium solutions showed excellent agreement with experimental data for mobility of water and ions compared to experiment.⁴⁷ Therefore, we have great confidence that the predicted water and hydroxide vehicular diffusion in AEMs are also quite reliable. In a previous study, Voth *et al.* found that vehicular mechanism contributes mainly to the dynamics of hydroxide in the confined water channels of related membranes,³⁵ although the role of Grotthuss mechanism on conductivity was not thoroughly investigated. Similarly, coarse-grained simulations of PPO-based AEM utilizing non-reactive force fields assumed that the vehicular motion of hydroxide is the dominant mechanism for the charge transport in these systems.^{45,67} Therefore, we can use hydroxide diffusion coefficients from our AEM simulations and estimate the expected ionic conductivity. However, we found that conductivity estimated based on the vehicular mobility of

fields has demonstrated the importance of the Grotthuss mechanism in allowing the OH⁻ to transport through the narrow bottlenecks in confined environment of water channel.³⁸ In that work, we have demonstrated this point by doing a head-to-head comparison of MD simulations using APPLE&P force field (only vehicular mechanism) and ReaxFF model (explicitly includes Grotthuss) for the same PPO-based membrane morphology. It was shown that the diffusivity of OH⁻ with the Grotthuss mechanism is much faster than when just the vehicular motion is involved. The difference was more than one order of magnitude. While in bulk water the difference between vehicular and Grotthuss mechanisms for OH⁻ transport is about factor of 2-3, in confined environments like investigated here, this difference is magnified.

Taking into account the discussed above morphology of water domains, *i.e.* the presence of larger water-rich domains interconnected with narrower bottleneck bridges, it is unlikely to expect that the Grotthuss mechanism can significantly contribute to the charge transport inside large water domains where the hydroxide anion is experiencing almost a bulk water-like environment and hence the contribution of the vehicular mechanisms should be dominating. However, when crossing the bottlenecks between the water rich domains the role of Grotthuss mechanism can be very significant. In such environments, the charge transport more resembles the

conditions of narrow 1D channels where previous ab initio MD simulations showed that Grotthuss mechanism dominates the transport.^{36,37} If the Grotthuss mechanism was present in our simulations, then the anion shown in Figure 12 would not have to wait for almost 5 ns to overcome a high free energy barrier associated with its partial dissolution upon transition through the narrow bottleneck. Instead, the proton hopping would facilitate the transition of hydroxide to the other side of the bottleneck.³⁸ In ref. 38 we showed, that the presence of the Grotthuss mechanisms allows the hydroxide to transition through bottlenecks without the need to partially lose its hydration structure. Figure S11 in the SI illustrates the difference in mechanisms of OH⁻ transition through a bottleneck as obtained from simulations using APPLE&P and ReaxFF force fields. Figure S12 illustrates transition of a water molecule through bottleneck.

Design of optimal cationic groups for PPO-based AEM.

Based on the discussion above, it is clear that optimal polymer architecture should lead to the formation of a continuous network of reasonably wide channels with minimum amount of bottlenecks connecting them. By adjusting the chemical structure of cationic groups, specifically by controlling the distribution of alkyl groups, one can control both the hydrophobicity/hydrophilicity of the side chain and the morphology of resulting water domains both of which strongly influence the hydration and mobility of OH⁻. Starting from the initial structure of 3R₁, general guidelines for optimizing the structure of the functional group for PPO-based AEM can be derived. From the analysis of pore-size distribution, we demonstrated introduction of more hydrophobic groups enhances the nanophase separation and provides the opportunity to increase the size of water domains, leading to water channels with larger pore sizes. However, there exists a delicate balance between introducing more hydrophobicity and maintaining the hydrophilicity. For example, in 3R₃, the propyl groups shield the cationic nitrogen, leading to a significantly reduced N⁺-O_w correlation (which will likely lead to an improved electrochemical stability), yet the enhanced nano-phase separation actually leads to disconnection between water domains. The asymmetrically modified 2R₁R₄ group which has a coexistence of hydrophilic alpha carbon and hydrophobic long alkyl chains, still yielded the increased size of water domains but created noticeably fewer bottlenecks between them therefore facilitating hydroxide diffusion. Introduction of hydrophilic moieties to the long alkyl tail, as in 2R₁R₅, led to reduced nanophase separation and while in this case we did not see a formation of obvious bottlenecks, the hydrophilic ether group was interfering with hydroxide mobility through those relatively uniform albeit narrow channels.

In conclusion, an optimal polymer structure for PPO-based AEM requires a delicate balance of hydrophilic and hydrophobic characters in functional groups that provide desired nanophase segregation and minimizes the amount of bottlenecks between water-rich domains. We believe that this can be achieved by utilizing asymmetric cationic groups, *e.g.* 2R₁R₄.

Author Information

Corresponding Author

* E-mail: d.bedrov@utah.edu

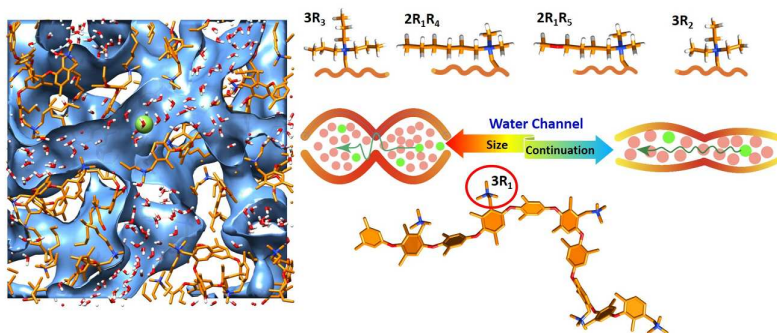
Conflicts of interest

The authors declare no competing financial interest.

Acknowledgement

The first two authors contributed equally to this work. The authors gratefully acknowledge the support from the project sponsored by the Army Research Laboratory under Cooperative Agreement Number W911NF-12-2-0023. The views and conclusions contained in this document are those of the authors and should not be interpreted as representing the official policies, either expressed or implied, of ARL or the U.S. Government. The U.S. Government is authorized to reproduce and distribute reprints for Government purposes notwithstanding any copyright notation herein. We also would like to acknowledge the Center of High Performance Computing at the University of Utah for technical support and generous allocation of computing resources.

TOC image



REFERENCES

- 1 Y. Wang, K. S. Chen, J. Mishler, S. C. Cho and X. C. Adroher, *Appl. Energy*, 2011, **88**, 981–1007.
- 2 M. Z. Jacobson, W. G. Colella and D. M. Golden, *Science*, 2005, **308**, 1901–1905.
- 3 L. Wang, E. Magliocca, E. L. Cunningham, W. E. Mustain, S. D. Poynton, R. Escudero-Cid and D. K. Whelligan, *Green Chem.*, 2017, **19**, 831–843.
- 4 K. D. Kreuer, *Chem. Mater.*, 2014, **26**, 361–380.
- 5 M. K. Debe, *Nature*, 2012, **486**, 43–51.
- 6 P. G. Grimes, *IEEE The Fifteenth Annual*, 2000, **15**, 41–45.
- 7 N. J. Robertson, H. A. Kostalik IV, T. J. Clark, P. F. Mutolo, H. D. Abruña and G. W. Coates, *J. Am. Chem. Soc.*, 2010, **132**, 3400–3404.
- 8 M. G. Marino, J. P. Melchior, A. Wohlfarth and K. D. Kreuer, *J. Membr. Sci.*, 2014, **464**, 61–71.
- 9 M. Mamlouk, J. A. Horsfall, C. Williams and K. Scott, *Int. J. Hydrogen Energy*, 2012, **37**, 11912–11920.
- 10 J. R. Varcoe, P. Atanassov, D. R. Dekel, A. M. Herring, M. A. Hickner, P. A. Kohl and T. Xu *Energy Environ. Sci.*, 2014, **7**, 3135–3191.
- 11 S. Maurya, S. H. Shin, Y. Kim, S. H. Moon, *Rsc Adv.* 2015, **5**, 37206–37230.
- 12 J. R. Varcoe and R. C. Slade, *Fuel cells*, 2005, **5**, 187–200.
- 13 G. Merle, M. Wessling and K. Nijmeijer, *J. Membr. Sci.* 2011, **377**, 1–35.
- 14 K. D. Kreuer, S. J. Paddison, E. Spohr and M. Schuster, *Chem. Rev.*, 2004, **104**, 4637–4678.
- 15 A. A. Shah, K. H. Luo, T. R. Ralph and F. C. Walsh, *Electrochim. Acta*, 2011, **56**, 3731–3757.
- 16 R. Jorn, J. Savage and G. A. Voth, *Acc. Chem. Res.* 2012, **45**, 2002–2010.
- 17 L. J. Abbott and A. L. Frischknecht, *Macromolecules*, 2017, **50**, 1184–1192.
- 18 J. Pan, C. Chen, L. Zhuang and J. Lu, *Acc. Chem. Res.*, 2011, **45**, 473–481.
- 19 J. Pan, C. Chen, Y. Li, L. Wang, L. Tan, G. Li and L. Zhuang, *Energy Environ. Sci.*, 2014, **7**, 354–360.
- 20 Y. L. Tse, H. N. Sarode, G. E. Lindberg, T. A. Witten, Y. Yang, A. M. Herring and G. A. Voth, *J. Phys. Chem. C*, 2013, **118**, 845–853.
- 21 Y. L. Tse, G. A. Voth, T. A. Witten and *J. Chem. Phys.*, 2015, **142**, 184905.
- 22 K. W. Han, K. H. Ko, K. Abu-Hakme, C. Bae, Y. J. Sohn and S. S. Jang *J. Phys. Chem. C*, 2014, **118**, 12577–12587.
- 23 D. C. Herbst, T. A. Witten, T. H. Tsai, E. B. Coughlin, A. M. Maes and A. M. Herring, *J. Chem. Phys.*, 2015, **142**, 114906.
- 24 J. Wang, Z. Zhao, F. Gong, S. Li and S. Zhang, *Macromolecules*, 2009, **42**, 8711–8717.
- 25 M. R. Hibbs, M. A. Hickner, T. M. Alam, S. K. McIntyre, C. H. Fujimoto and C. J. Cornelius, *Chem. Mater.*, 2008, **20**, 2566–2573.
- 26 J. R. Varcoe and R. C. Slade, *Fuel cells*, 2005, **5**, 187–200.
- 27 J. Ran, L. Wu, Y. He, Z. Yang, Y. Wang, C. Jiang and T. Xu. *J. Membr. Sci.*, 2017, **522**, 267–291.
- 28 B. Zhang, S. Gu, J. Wang, Y. Liu, A. M. Herring and Y. Yan, *RSC Adv.*, 2012, **2**, 12683–12685.
- 29 M. T. Kwasny, G. N. Tew, *J. Mater. Chem. A*, 2017, **5**, 1400–1405.
- 30 J. Han, L. Zhu, J. Pan, T. J. Zimudzi, Y. Wang, Y. Peng and L. Zhuang, *Macromolecules*, 2017, **50**, 3323–3332.
- 31 L. Zhu, J. Pan, Y. Wang, J. Han, L. Zhuang and M. A. Hickner, *Macromolecules*, 2016, **49**, 815–824.
- 32 W. Zhang and A. C. van Duin, *J. Phys. Chem. C*, 2015, **119**, 27727–27736.
- 33 S. J. Peighambardoust, S. Rowshanzamir and M. Amjadi, *Int. J. Hydrogen Energy*, 2010, **35**, 9349–9384.
- 34 K. N. Grew and W. K. Chiu, *J. Electrochem. Soc.*, 2010, **157**, B327–B337.
- 35 C. Chen, Y. L. Tse, G. E. Lindberg, C. Knight and G. A. Voth, *J. Am. Chem. Soc.*, 2016, **138**, 991–1000.
- 36 A. Bankura and A. Chandra, *J. Phys. Chem. B*, 2012, **116**, 9744–9757.
- 37 M. Rossi, M. Ceriotti and D. E. Manolopoulos, *J. Phys. Chem. Lett.*, 2016, **7**, 3001–3007.
- 38 D. Dong, W. Zhang, A. C. van Duin, D. Bedrov, *J. Phys. Chem. Lett.* 2018, **9**, 825–829.
- 39 O. Borodin, *J. Phys. Chem. B*, 2009, **113**, 11463–11478.
- 40 D. Bedrov, O. Borodin, Z. Li and G. D. Smith, *J. Phys. Chem. B*, 2010, **114**, 4984–4997.
- 41 Y. Wang, L. Xing, W. Li and D. Bedrov, *J. Phys. Chem. Lett.*, 2013, **4**, 3992–3999.
- 42 L. Xing, J. Vatamanu, O. Borodin, G. D. Smith and D. Bedrov, *J. Phys. Chem. C*, 2012, **116**, 23871–23881.
- 43 O. N. Starovoytov, O. Borodin, D. Bedrov and G. D. Smith, *J. Chem. Theory Comput.*, 2011, **7**, 1902–1915.
- 44 X. Wei, J. B. Hooper and D. Bedrov, *Liq. Cryst.*, 2016, **44**, 332–347.
- 45 N. Li, Y. Leng, M. A. Hickner and C. Y. Wang, *J. Am. Chem. Soc.*, 2013, **135**, 10124–10133.
- 46 V. Lesch, Z. Li, D. Bedrov, O. Borodin and A. Heuer, *Phys. Chem. Chem. Phys.*, 2016, **18**, 382–392.
- 47 D. Dong, J. B. Hooper and D. Bedrov, *J. Phys. Chem. B*, 2017, **121**, 4853–4863.
- 48 P. J. Stephens, F. J. Devlin, C. Chabalowski and M. J. Frisch, *J. Phys. Chem.*, 1994, **98**, 11623–11627.
- 49 M. P. McGrath and L. Radom, *J. Chem. Phys.*, 1991, **94**, 511–16.
- 50 I. S. Ufimtsev, A. G. Kalinichev, T. J. Martinez and R. J. Kirkpatrick, *Chem. Phys. Lett.*, 2007, **442**, 128–133.
- 51 C. D. Wick and L. X. Dang, *J. Phys. Chem. A*, 2009, **113**, 6356–6364.
- 52 S. Kale and J. Herzfeld, *Angew. Chem. Int. Ed.*, 2012, **51**, 11029–11032.
- 53 P. Atkins and J. De Paula, *Atkins's Physical Chemistry Seventh Edition*. Oxford University Press, USA, 2001
- 54 Y. Zhao, N. E. Schultz and D. G. Truhlar, *J. Chem. Theory and Comput.*, 2006, **2**, 364–382.
- 55 T. H. Dunning Jr., *J. Chem. Phys.*, 1989, **90**, 1007–1023.
- 56 M. Rossi, M. Ceriotti and D. E. Manolopoulos, *J. Phys. Chem. Lett.*, 2016 **7**, 3001–3007.
- 57 B. T. Thole, *Chem. Phys.*, 1981, **59**, 341–350.
- 58 B. J. Palmer, *J. Comput. Phys.*, 1993, **104**, 470–472.
- 59 Y. Koga, F. Sebe and K. Nishikawa, *J. Phys. Chem. B*, 2013, **117**, 877–883.
- 60 E. F. Pettersen, T. D. Goddard, C. C. Huang, G. S. Couch, D. M. Greenblatt, E. C. Meng and T. E. Ferrin, *J. Comput. Chem.*, 2004, **25**, 1605–1612.
- 61 Y. Pan, Q. Zhang, X. Yan, J. Liu, X. Xu, T. Wang, G. He, *J. Membr. Sci.*, 2018, **552**, 286–284.

62 S. Bhattacharya and K. E. Gubbins, *Langmuir*, 2006, **22**, 7726-7731.

63 G. Williams and D. Watts, *Trans. Faraday Soc.*, 1970, **66**, 80-85.

64 H. N. Sarode, G. E. Lindberg, Y. Yang, L. E. Felberg, G. A. Voth and A. M. Herring *J. Phys. Chem. B.*, 2014 **118**, 1363-1372.

65 L. Garcia-Tarres and E. Guardia, *J. Phys. Chem. V*, 1998, **102**, 7448-7454.

66 W. Kob, C. Donati, S. J. Plimpton, P. H. Poole and S. C. Glotzer, *Phys. Rev. Lett.*, 1997, **79**, 2827.

67 J. Lu, L. C. Jacobson, Y. A. Perez Sirkin and V. Molinero, *J. Chem. Theory Comput.*, 2016, **13**, 245-264.

68 H. S. Dang, E. A. Weiber and P. Jannasch, *J. Mater. Chem. A*, 2015, **3**, 5280-5284.